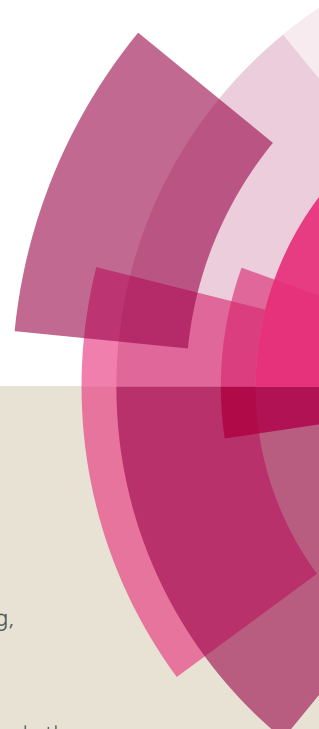
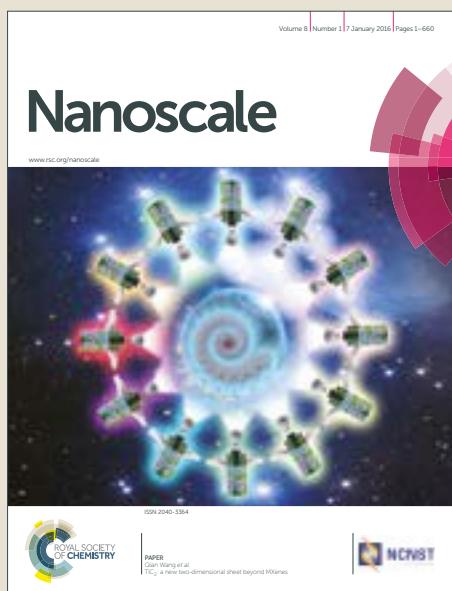


# Nanoscale

Accepted Manuscript



This article can be cited before page numbers have been issued, to do this please use: G. Gao, Y. Xiang, S. Lu, B. Dong, S. Chen, L. Shi, Y. Wang, H. Wu, Z. Li, A. Abdelkader, S. Ding and K. Xi, *Nanoscale*, 2017, DOI: 10.1039/C7NR05407F.



This is an Accepted Manuscript, which has been through the Royal Society of Chemistry peer review process and has been accepted for publication.

Accepted Manuscripts are published online shortly after acceptance, before technical editing, formatting and proof reading. Using this free service, authors can make their results available to the community, in citable form, before we publish the edited article. We will replace this Accepted Manuscript with the edited and formatted Advance Article as soon as it is available.

You can find more information about Accepted Manuscripts in the [author guidelines](#).

Please note that technical editing may introduce minor changes to the text and/or graphics, which may alter content. The journal's standard [Terms & Conditions](#) and the ethical guidelines, outlined in our [author and reviewer resource centre](#), still apply. In no event shall the Royal Society of Chemistry be held responsible for any errors or omissions in this Accepted Manuscript or any consequences arising from the use of any information it contains.



Journal Name

COMMUNICATION

## CTAB-assisted growth of self-supported Zn<sub>2</sub>GeO<sub>4</sub> nanosheets network on a conductive foam as a binder free electrode for long-life lithium ion batteries

Received 00th January 20xx,  
Accepted 00th January 20xx

DOI: 10.1039/x0xx00000x

www.rsc.org/

Guoxin Gao,<sup>a†</sup> Yang Xiang,<sup>a†</sup> Shiyao Lu,<sup>a</sup> Bitao Dong,<sup>a</sup> Sheng Chen,<sup>a</sup> Lei Shi,<sup>a</sup> Yuankun Wang,<sup>a</sup> Hu Wu,<sup>a</sup> Zhaoyang Li,<sup>a</sup> Amr Abdelkader,<sup>cd</sup> Kai Xi<sup>\*b</sup> and Shujiang Ding<sup>\*a</sup>

Ge-based compounds show great potential as replacements for traditional graphite anode in lithium-ion batteries (LIBs). However, large volume changes and the low conductivity of such materials result in poor electrochemical cycling and rate performance. Here we fabricate a self-supported, three-dimensional (3D) sponge-like structure of interlinked Zn<sub>2</sub>GeO<sub>4</sub> ultrathin nanosheets anchored vertically on nickel foam (ZGO NSs@NF) via a simple hydrothermal process assisted by cetyltrimethyl ammonium bromide (CTAB). Such robust self-supported hybrid structures greatly improve the structural tolerance of active materials and accommodate the volume variation that occurs during repeated electrochemical cycling. As expected, the self-supported ZGO NSs@NF composites demonstrate excellent lithium storage with a high discharge capacity, long cycling life and good rate capability when used as binder-free anodes for LIBs. A high reversible discharge capacity of 794 mAh g<sup>-1</sup> is maintained after 500 cycles at 200 mA g<sup>-1</sup>, corresponding to 81% capacity retention of the second cycle. Further evaluation at a higher current density (2 A g<sup>-1</sup>) also delivers a reversible discharge capacity (537 mAh g<sup>-1</sup>) for this binder-free anode. This novel 3D structure of self-supported ultrathin nanosheets on a conductive substrate, with its volume buffer effect and good interfacial contacts, can stimulate the progress of other energy-efficient technologies.

### Introduction

Lithium ion batteries (LIBs) are considered to be one of the most promising power sources for portable electronic devices, plug-in hybrid electric vehicles (HEVs) and stationary grid applications due to their high energy densities, long-term cycling stability, no memory effects and eco-friendliness.<sup>1-4</sup> One challenge that faces the further development of high-performance LIBs is the limited capacity of graphite negative electrodes (372 mAh g<sup>-1</sup>).<sup>2-5,6</sup> Tremendous efforts have been made to develop new anode materials that could replace traditional graphite anodes, including using group IV elements (silicon, germanium and tin),<sup>7-10</sup> and transition metal oxides/sulfides.<sup>11-18</sup> Among them, special attention has been

paid to Ge-based anodes due to their high theoretical specific capacities (ca. 1600 mAh g<sup>-1</sup>) by forming the alloy Li<sub>4.4</sub>Ge, fast Li<sup>+</sup> diffusivity (400 times faster than Si) and good electric conductivity (almost 100 times higher than Si).<sup>19-25</sup> However, like most metal-based electrodes, pure Ge anodes are expensive and suffer from rapid capacity decays caused by the large volume changes (about 370%) that occur between the lithium alloying and de-alloying process.<sup>23-25</sup>

The exploration of stable and high-capacity ternary metal germinate compounds has the great potential to improve electrochemical cycling performances and reduce the fabrication costs of Ge-based anodes. Partially substituting expensive Ge with cheaper metal elements such as Zn, Cu, Fe, Cd, Ca and Co in the ternary oxide structure could generate a moderate buffer zone to accommodate volume variation of electrode materials by means of the favorable synergistic effect and simultaneously improve electrode electrochemical performance.<sup>26-39</sup> Ternary Zn<sub>2</sub>GeO<sub>4</sub>-based anodes have been well studied in literature and they can deliver a high theoretical capacity of 1443 mAh g<sup>-1</sup> based on conversion and lithium alloying reactions (Zn<sub>2</sub>GeO<sub>4</sub> + 8 Li<sup>+</sup> + 8 e<sup>-</sup> → 2 Zn + Ge + 4 Li<sub>2</sub>O, Ge + 4.4 Li<sup>+</sup> + 4.4 e<sup>-</sup> ↔ Li<sub>4.4</sub>Ge, Zn + Li<sup>+</sup> + e<sup>-</sup> ↔ LiZn).<sup>40</sup> Despite significant efforts, the practical application of such Zn<sub>2</sub>GeO<sub>4</sub>-based anodes is still hampered by their fast capacity fading and poor rate capability, which can be ascribed to their intrinsic poor electronic conductivity and large volumetric variation upon cycling.<sup>41-43</sup> Meanwhile, severe pulverization and structural collapse of the electrodes, significant aggregation of the intermediates, and subsequent detachment of the active

<sup>a</sup> Department of Applied Chemistry, School of Science, Xi'an Jiaotong University, Xi'an 710049, P. R. China. E-mail: dingsj@xjtu.edu.cn

<sup>b</sup> Department of Materials Science and Metallurgy, University of Cambridge, Cambridge CB3 0FS, United Kingdom. E-mail: kx210@cam.ac.uk

<sup>c</sup> National Graphene Institute (NGI), University of Manchester, Booth Street East, Manchester, M13 9QS, United Kingdom.

<sup>d</sup> Faculty of Science and Technology, Bournemouth University, Poole House, Talbot Campus, Poole, Dorset, BH12 5BB

<sup>†</sup> These authors contributed equally to this work.

†Electronic Supplementary Information (ESI) available: Experimental sections; Digital picture, XRD and EDX patterns of ZGO NSs@NF; FESEM images of ZGO NRs@NF, pristine ZGO flakes and ZGO NRs; Nyquist plots of ZGO NSs@NF, ZGO NRs@NF and pristine ZGO flakes; and post-mortem FESEM images of ZGO NRs@NF. See DOI: 10.1039/x0xx00000x

materials from the current collector are also responsible for limiting the electrochemical cycling performance of  $\text{Zn}_2\text{GeO}_4$ -based anodes.<sup>44, 45</sup>

As shown in **Figure 1A-C**, directly growing electroactive materials with well-designed nanostructures (0D, 1D, 2D and 3D) on conductive substrates as binder-free electrodes has become an effective strategy for enhancing the battery cycling stability and rate capability.<sup>46-49</sup> The improvement in cycling stability is due to enhanced electronic conductivity and interfacial contacts between the current collector and the active materials compared with the simple physical mixing. For example, Wang and co-workers synthesized carbon coated coaxial  $\text{Zn}_2\text{GeO}_4$  nanowires on copper foil as the anode material, which exhibits a remarkably stable discharge capacity of  $790 \text{ mAh g}^{-1}$  after 100 cycles.<sup>50</sup> Subsequently, they grew a carbon-coated  $\text{Zn}_2\text{GeO}_4$  particle film on a nickel foam as a

binder-free anode for LIBs.<sup>51</sup> Shen and co-workers also reported a good cycling stability for anodes engineered from metal germanate nanowires such as  $\text{Ca}_2\text{Ge}_7\text{O}_{16}$ ,  $\text{SrGe}_4\text{O}_9$ ,  $\text{BaGe}_4\text{O}_9$ , and  $\text{Zn}_2\text{GeO}_4$  grown on carbon textiles.<sup>39, 52</sup> To the best of our knowledge, the reported morphologies of metal germanate compounds in the literature mainly include nanoparticles, nanorods and nanowires.<sup>37-45, 53-59</sup> Compared with the reported morphologies, the free-standing ultrathin nanosheets with an interlinked self-supported network aligning on a conductive substrate usually offer a more robust mechanical structure as well as better electrolyte diffusion within the electrode, a larger exposed specific surface area and more abundant active sites to carry out the electrochemical reactions, thus can deliver good electrochemical performance.<sup>13, 14, 60</sup>

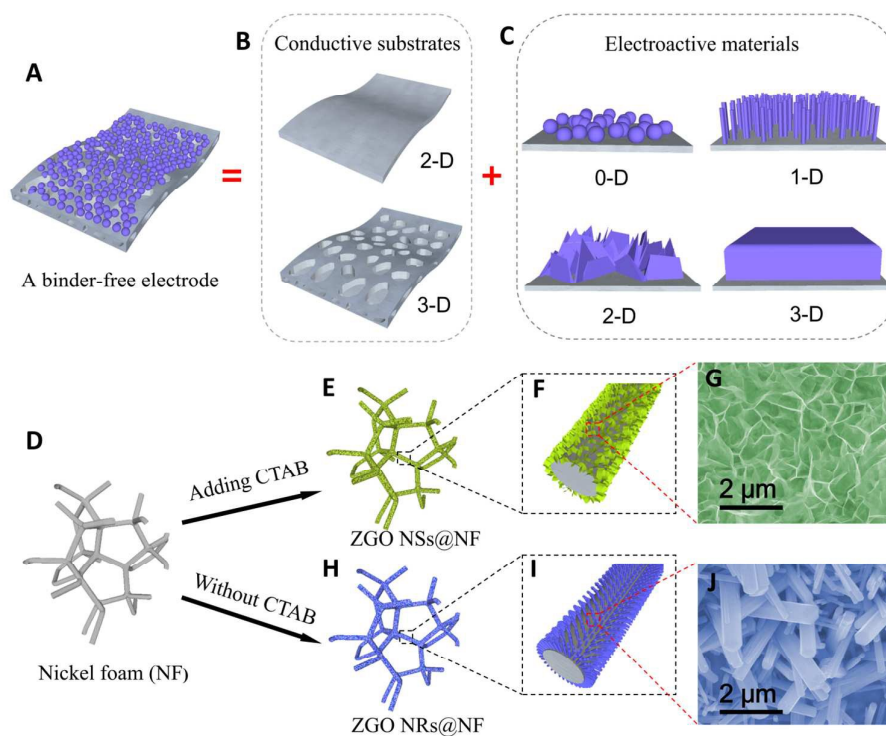


**Figure 1.** Schematic illustration of a binder-free electrode and the influence of CTAB on the morphology of the hierarchical hybrid  $\text{ZGO NSs@NF}$  and  $\text{ZGO NRs@NF}$ .

In this work, we successfully develop a novel hierarchical hybrid nanostructure of free-standing ultrathin  $\text{Zn}_2\text{GeO}_4$  nanosheets anchored on nickel foam (NF) substrates (denoted as  $\text{ZGO NSs@NF}$ ) via a simple hydrothermal process assisted by cetyltrimethyl ammonium bromide (CTAB) as schematically illustrated in **Figure 1D-J**. The free-standing ultrathin  $\text{ZGO NSs}$  are interconnected to demonstrate a 3D self-supported sponge-like structure, which uniformly covers the conductive NF substrate. When used as binder-free anodes for LIBs directly, the self-supported  $\text{ZGO NFs@NF}$  composites demonstrate highly enhanced electrochemical performance due to their large surface area, high porosity, and robust structural tolerance. A high reversible discharge capacity of about  $793 \text{ mAh g}^{-1}$  has been successfully maintained after 500 cycles at a current density of  $200 \text{ mA g}^{-1}$ , corresponding to about an 81% reversible discharge capacity retention of the second cycle. Even when cycled at a higher current density of  $2 \text{ A g}^{-1}$ , the

self-supported  $\text{ZGO NSs@NF}$  anodes still deliver a stable discharge capacity of about  $537 \text{ mAh g}^{-1}$ , exhibiting an excellent rate capability.

## Results and discussion

**Figure 2A** shows the digital picture of NF substrate and as-prepared 3D self-supported  $\text{ZGO NSs@NF}$  composites. Obviously, after the simple CTAB-assisted hydrothermal process, the surface of NF substrate becomes darker, confirming the successful growth of  $\text{ZGO}$  layer on NF substrate. Remarkably, binding, stretching and twisting the composite electrode does not result in visible changes to black powder peeling from the substrate as can be seen in **Figure S1** (see Supporting Information). The X-ray diffraction (XRD) patterns

of the as-prepared self-supported ZGO NSs@NF are shown in **Figure S2** (see Supporting Information) to distinguish their crystallographic structure and phase purity. Except for the three characteristic diffraction peaks derived from the NF substrate (JCPDS no. 04-0850), all the other diffraction peaks are indexed to the rhombohedral  $\text{Zn}_2\text{GeO}_4$  crystalline structure (JCPDS no. 11-0687).<sup>43, 61</sup> No additional peaks can be found, which strongly suggests that the self-supported ZGO NSs@NF

composites have a high purity. More importantly, the energy dispersive X-ray (EDX) analysis as shown in **Figure S3** (see Supporting Information) further confirms that the self-supported hybrid composites are mainly composed of Ni, Zn, Ge and O elements, and the atomic ratio (At%) of Zn: Ge is close to 2:1. The Ni elements in the EDX plot are from the NF substrate.

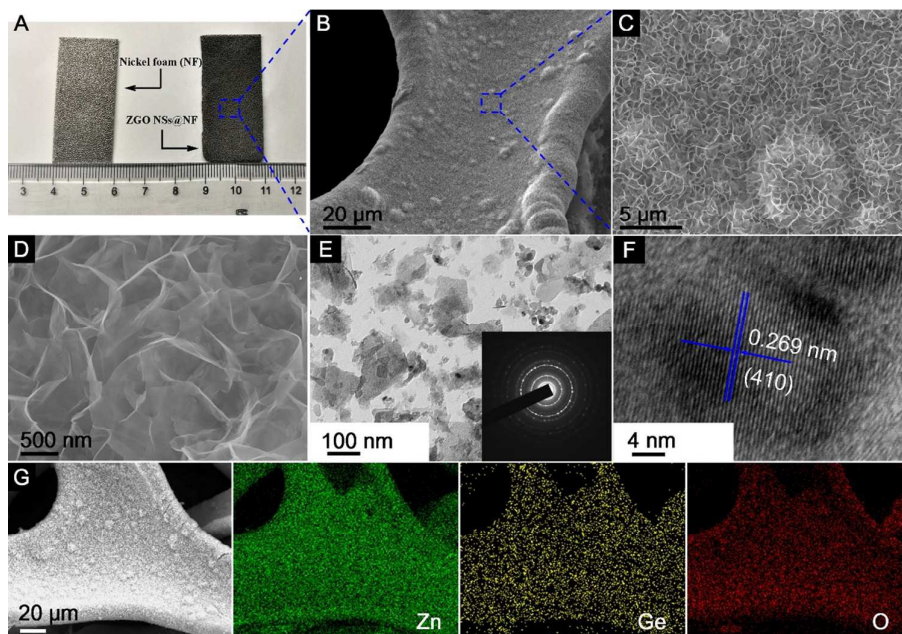


**Figure 2.** (A) Digital photo, (B–D) FESEM, (E) TEM, (F) HRTEM images and (G) EDX–element mapping of the ZGO NSs@NF obtained through CTAB-assisted hydrothermal reaction at 160 °C for 180 min. The inset image in E shows the SAED pattern.

The morphologies of as-prepared ZGO NSs@NF are examined by field-emission scanning electron microscopy (FESEM), transmission electron microscopy (TEM) and high-resolution TEM (HRTEM) as shown in **Figure 2B–F**. **Figure 2B** shows the morphology of the novel ZGO NSs@NF at low magnification. The coating seems to be homogeneous with no clear aggregations of ZGO NSs on the NF substrate. At higher magnification, **Figure 2C** and **2D** distinctly reveal those ultrathin ZGO NSs are interconnected each other and arranged in a 3D sponge-like network. Such an interlinked porous structure is self-supported and firmly anchored on the conductive substrate. However, when we repeated the experiment without placing NF substrate in the hydrothermal system, only a few pristine ZGO nanoflakes are obtained as shown in **Figure S4A** and **S4B** (see Supporting Information). Additionally, close observation (**Figure S4B**) reveals that most ZGO nanoflakes are stacking together to form clusters, which means one of the roles of NF is to prevent the aggregation of ultrathin ZGO flakes. To obtain more detailed microstructural information, the self-supported ZGO interlinked NSs are exfoliated from NF by ultrasonication in ethanol, and then dripped directly onto a copper grid to carry out TEM analysis. **Figure 2E** shows that the flake size of the exfoliated ZGO NSs is around 200 nm. We believe that the actual flake size on the NF substrate is much greater than 200 nm. Due to the strong adhesion between ZGO NSs and the NF substrate, extensive sonication was required, resulting in breaking the ZGO flakes into smaller fragments. The polycrystalline nature of the rhombohedral  $\text{Zn}_2\text{GeO}_4$  phase is also confirmed by the

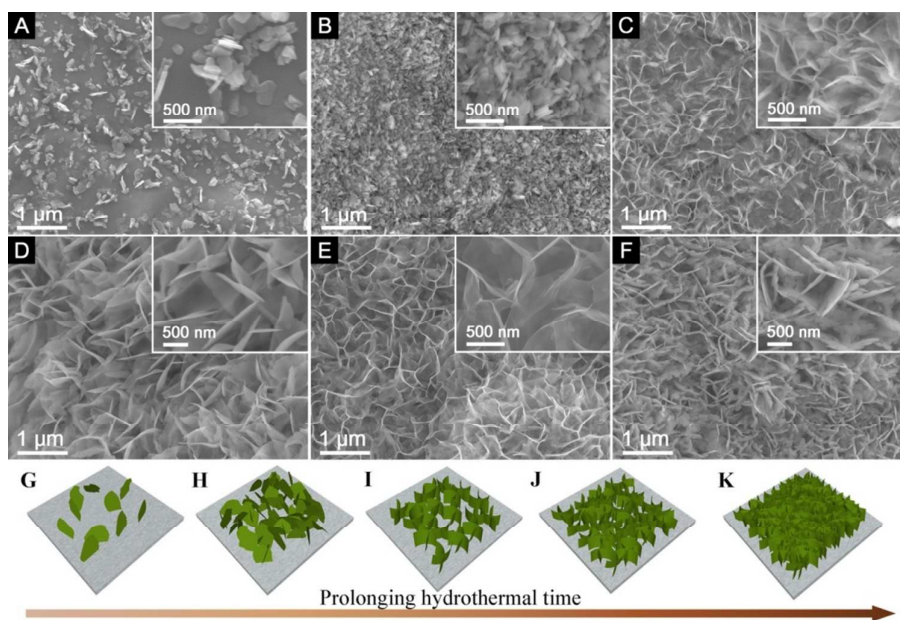
intermittent diffraction rings shown in the insert of **Figure 2E**. In addition, the structural feature of a typical ZGO NS fragment with visible lattice fringes has been observed in an HRTEM image (**Figure 2F**). The marked interplanar distance of 0.269 nm corresponds to the (410) crystal planes of the rhombohedral  $\text{Zn}_2\text{GeO}_4$  phase. Element mapping further confirms the chemical components of as-prepared ZGO NSs@NF composites (**Figure 2G**). All the key elements, including Zn, Ge and O, are detected distinctly with homogeneous distribution throughout the measurement area.

We find that the CTAB surfactant plays a crucial role in the successful formation of the 3D self-supported ZGO NSs on an NF substrate. We have conducted several experiments with different amounts of CTAB added during the hydrothermal reaction. The FESEM images of as-synthesized materials are shown in **Figure S5** (see Supporting Information). **Figure S5A** shows the products of the hydrothermal process without CTAB addition. Clearly, only short ZGO nanorods (NRs) with a hexagonal cross-section can be detected on the NF (denoted as ZGO NRs@NF), but these free-standing ZGO NRs anchored on NF surface are isolated from each other. When adding a little amount (0.3 mmol) of CTAB into this hydrothermal system, most free-standing ZGO NRs disappear and are transferred into small sheet-like protuberances covering on NF surface as shown in **Figure S5B**. Further increasing the amount of CTAB to 0.7 mmol, the sheet-like tiny protuberances have grown into interconnected ZGO NSs, which are free-standing anchored on NF support (**Figure S5C**). Meanwhile, less and less rod-like structure of ZGO NRs could be observed,

suggesting that CTAB has an important influence on the formation of ultrathin ZGO NSs with a self-supported structure in this work. We believe that the adsorption of CTAB molecules on some facets of crystalline ZGO subunits significantly lowers their surface free energy and drives the formation of the sheet-like nanostructure on NF.<sup>62</sup> Similar phenomenon was observed in the fabrication silver nanoplates.<sup>63</sup> However, as can be seen from **Figure S5D**, even when the amount of CTAB is increased to 2 mmol, we still only obtain the ultrathin ZGO NSs anchored on NF substrate. Therefore, we chose 1 mmol as the optimal amount of CTAB in this research.

To further understand the growth mechanism of the self-supported ZGO NSs@NF, we collected a series of samples at different intervals in the hydrothermal process and investigated their morphologies using FESEM as shown in **Figure 3**. The ZGO flakes start to appear on the NF substrate in the initial few minutes of hydrothermal treatment (**Figure 3A**). These original

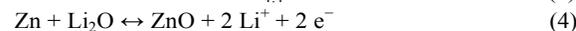
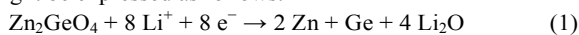
flakes work as seeds for further growth and it took only 30 min. of processing to fully cover the NF substrate with thin ZGO flakes (**Figure 3B**). The second layer, grown on the top of the first ZGO layer, seems to be composed of thinner flakes. The new flakes appear to be oriented vertically on the substrate as can be seen from the SEM image of the sample after 60 min. (**Figure 3C**). Longer processing times, 120 min. (**Figure 3D**) and 180 min. (**Figure 3E**), lead to a more ordered arrangement of these ultrathin flakes creating honeycomb-like structures with the ZGO flakes interlinked at the edges and aligned vertically on the NF support. However, prolonged treatment (such as 240 min.) leads to excessive growth of the thin ZGO flakes in a direction parallel to the substrate, thus showing the increasing flake thickness (**Figure 3F**). Therefore, we settled on an ideal hydrothermal period of 180 min at 160 °C to obtain the self-supported ZGO NSs@NF composites. The gradual evolution process is illustrated schematically in **Figure 3G-K**.



**Figure 3.** FESEM images of ZGO@NF products obtained at 160 °C for various hydrothermal times: (A) 10 min, (B) 30 min, (C) 60 min, (D) 120 min, (E) 180 min and (F) 240 min.

Next we carried out CV measurements at a scanning rate of 0.5 mV s<sup>-1</sup> in the voltage window of 0.01-3 V vs. Li/Li<sup>+</sup> to identify the electrochemical reactions of self-supported ZGO NSs@NF composites by directly using them as binder-free anodes for LIBs. As shown in **Figure 4A**, the initial CV scan is very different from subsequent ones, but there are no apparent differences from the second cycle onwards, especially in the charge branch. In the initial cathodic sweep, two reduction peaks can be observed on the CV plots. The predominant peak located at about 0.63 V may be ascribed to the decomposition of Zn<sub>2</sub>GeO<sub>4</sub> into Zn, Ge, Li<sub>2</sub>O and the formation of a solid electrode interface (SEI) film, as well as the partial degradation of organic electrolyte.<sup>38, 64</sup> Another relatively peak at round 0.31 V can be attributed to the alloying reactions of Zn-Li and Ge-Li.<sup>50, 55</sup> Compared with the reduction peak in the first cycle, the strong reduction peak at 0.63 V shifts to a higher voltage (about 0.84 V) in the second cycle and then moves back slightly to a lower

voltage again in the third cycle.<sup>51</sup> In the anodic sweep process, a distinct oxidation peak can be detected at about 1.39 V corresponding to the reoxidation of metallic Zn and Ge into ZnO and GeO<sub>2</sub>, respectively.<sup>42</sup> The weak and broad peak between 0.4 and 0.9 V was assigned to the delithiation reactions of the Li-metal alloys.<sup>50</sup> Therefore, according to the CV analysis and previously reported lithium-storage mechanisms of ZnO and GeO<sub>2</sub>, the corresponding electrochemical reactions for the ZGO NSs@NF anode might be expressed as follows.<sup>38, 40, 65</sup>



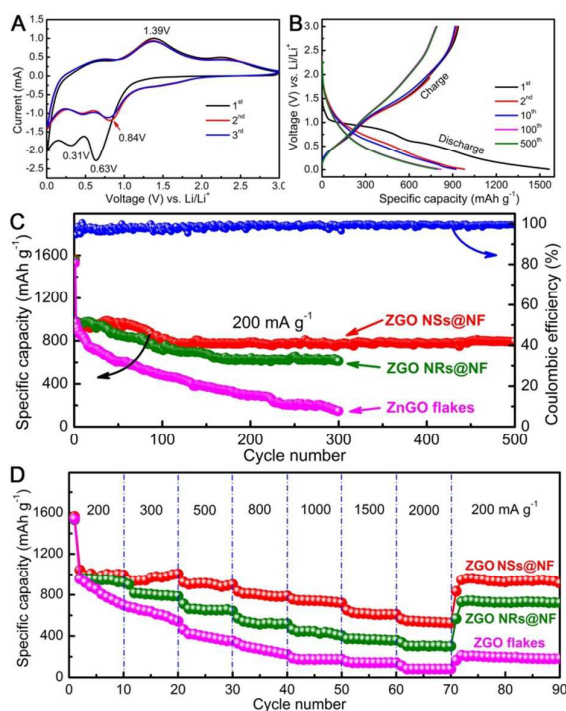


**Figure 4.** Electrochemical characterization: (A) CVs of ZGO NSs@NF tested at a scan rate of  $0.5 \text{ mV s}^{-1}$  between 0.01 and 3 V; (B) discharge-charge voltage profiles of ZGO NSs@NF at a current density of  $200 \text{ mA g}^{-1}$  in the cut-off voltage of 0.01–3 V; (C) cycling performance; and (D) rate capability of ZGO NSs@NF, ZGO NRs@NF and ZGO flakes evaluated at different current densities between 0.01 and 3 V.

The lithium storage properties were further investigated in a single half-cell using galvanostatic discharge/charge measurements. **Figure 4B** reveals the corresponding discharge/charge voltage profiles of the 1<sup>st</sup>, 2<sup>nd</sup>, 10<sup>th</sup>, 100<sup>th</sup> and 500<sup>th</sup> cycles of the binder-free ZGO NSs@NF electrode at a current density of  $200 \text{ mA g}^{-1}$  within the cut-off voltage of 0.01–3.0 V vs.  $\text{Li/Li}^+$ . For the first cycle, the self-supported ZGO NSs@NF electrode delivers high discharge and charge capacities of 1564 and  $928 \text{ mAh g}^{-1}$ , respectively, presenting an irreversible loss of about 40.7%. Such irreversible capacity loss in the first cycle is usually due to the possible decomposition of electrolyte, the formation of an SEI layer on the surface of the electrodes, an incomplete conversion reaction or irreversible lithium uptake.<sup>64</sup> The discharge plateaus at 0.2–1.0 V and the charge plateaus at 0.5–1.4 V observed in the discharge/charge curves can be attributed to the lithium alloying and de-alloying reactions.<sup>55</sup> All the data are in good agreement with the above-mentioned CV results and the literature.<sup>38, 50, 51</sup> From the second cycle onwards, the voltage profiles of self-supported ZGO NSs@NF anodes are nearly overlapping, indicating the reversibility of the electrochemical reactions. **Figure 4C** further compares the cycling properties of ZGO NSs@NF, ZGO NRs@NF and ZGO flakes at a current density of  $200 \text{ mA g}^{-1}$ . The self-supported ZGO NSs@NF anodes exhibit the best specific capacity and cycling stability in the three electrodes. The discharge capacities of this binder-free electrode consistently maintain a high and stable value of about  $794 \text{ mAh g}^{-1}$  even after 500 cycles at  $200 \text{ mA g}^{-1}$ , with

the exception of a slight increase before the initial 30 cycles. The gentle increase in capacity in the initial cycles implies a slow activation process, which might be related to the inadequate surface contact at the beginning of the measurement between electroactive ZGO NSs@NF and electrolyte.<sup>55</sup> Meanwhile, build-up of a stable SEI layer on the active materials also needs a certain number of cycles, which leads to a slight increase in the discharge capacity in the initial cycles.<sup>66</sup> It is worth noting from **Figure 4C** that the Coulombic efficiencies of the self-supported ZGO NSs@NF anodes are more than 98% after the initial cycles and remain almost unchanged in the subsequent cycles. The high Coulombic efficiencies highlight the excellent energy-conversion efficiency of the self-supported ZGO NSs@NF. Like the self-supported ZGO NSs@NF anode, the ZGO NRs@NF anode also presents good electrochemical cycling stability since the ZGO NRs are also anchored to a conductive NF substrate. However, the discharge capacities decrease slowly from  $983 \text{ mAh g}^{-1}$  for the second cycle and maintain a low value of about  $613 \text{ mAh g}^{-1}$  over 300 cycles. We believe that the relatively small specific surface area of the hybrid ZGO NRs@NF is responsible for making the discharge capacities lower than those of the self-supported ZGO NSs@NF.<sup>67</sup> However, without the support of the conductive NF, the pristine ZGO flakes demonstrate the poorest cycling stability compared with the other two binder-free electrodes. After the second cycle, the discharge capacity decreased over 300 cycles from  $971 \text{ mAh g}^{-1}$  to  $147 \text{ mAh g}^{-1}$  at the 300<sup>th</sup> cycle. To compare the rate capabilities of the three samples, the test cells were further evaluated at different current densities ranging from 200 to  $2000 \text{ mA g}^{-1}$  as shown in **Figure 4D**. The discharge capacities of ZGO NSs@NF and ZGO NRs@NF slowly decreased with increasing current densities. The ZGO NSs@NF and ZGO NRs@NF electrodes still deliver reversible discharge capacities of 537 and  $302 \text{ mAh g}^{-1}$ , respectively, at a current density of as high as  $2000 \text{ mA g}^{-1}$ . Both electrodes are able to recover high discharge capacities:  $938 \text{ mAh g}^{-1}$  for ZGO NSs@NF and  $722 \text{ mAh g}^{-1}$  for ZGO NRs@NF when the current densities fall back to  $200 \text{ mA g}^{-1}$ . However, the pristine ZGO flake electrode demonstrates a rather inferior rate capability compared to the other binder-free electrodes. It delivers a much lower discharge capacity of about  $82 \text{ mAh g}^{-1}$  at  $2000 \text{ mA g}^{-1}$ . Then the recovered discharge capacity is as low as  $180 \text{ mAh g}^{-1}$  with the current density returning back to  $200 \text{ mA g}^{-1}$ .

In order to explore the reaction kinetics of the as-prepared ZGO NSs@NF electrodes, CV measurements of ZGO NSs@NF anode at different scan rate were recorded as shown in **Figure S6A** (see Supporting Information). It is well known that the relation between current ( $i$ ) and the scanning rate ( $v$ ) can be described by the following equations s:<sup>68–70</sup>

$$i = av^b \quad (6)$$

$$\log(i) = b \log(v) + \log(a) \quad (7)$$

where  $a$  and  $b$  are both constants. The value of  $b$  is between 0.5 and 1.0, especially  $b=0.5$  means the electrochemical reaction is a diffusion-controlled process while  $b=1.0$  denotes a capacitive-controlled process. The  $b$  value could be obtained through fitting the slope of the  $\log(i)$  vs.  $\log(v)$  plot at every redox peak, which have been shown in **Figure S6B** (see Supporting Information). The values of the five redox peaks were 0.96, 0.79, 0.73, 0.85 and 0.92, implying that the redox reactions of ZGO NSs@NF electrodes during the charge-discharge are mainly controlled by the capacitive

process, thus leading to highly enhanced reversible capacity and excellent rate performance.

To mimicking the practical application of the ZGO NSs@NF electrode, we further assembled them into full-cells using commercial  $\text{LiFePO}_4$  as cathode and electrochemically pre-lithiated ZGO NSs@NF as anode. The loading mass ratio of  $\text{LiFePO}_4$  cathode and pre-lithiated ZGO NSs@NF anode was controlled about 4:1 in order to ensure the ZGO NSs@NF anode capacity exceed a little. The full-cells was charged and discharged at 0.2 C (1 C =  $170 \text{ mA h g}^{-1}$ , respect to  $\text{LiFePO}_4$ ) within the cut-off voltage of 2.0-3.8V. **Figure S7A** (see Supporting Information) showed the charge-discharge curves at 1, 2, 10 cycles. As can be seen, the initial discharge capacity was  $160 \text{ mA h g}^{-1}$  while the initial Coulombic efficiency was as high as 96.7%, suggesting superb reversible performance. Even after 80 cycles, the discharge capacity could still be remained at  $104 \text{ mA h g}^{-1}$  (**Figure S7B**, see Supporting Information). Clearly, the  $\text{LiFePO}_4/\text{ZGO NSs@NF}$  full-cells exhibit good capacity, cycling stability and high Coulombic efficiency. The electrochemical results of full-cells verified the potential of ZGO NSs@NF as a promising candidate for LIBs anode. In addition, to present the superior electrochemical performance of our well-designed self-supported ZGO NSs@NF composites, other reported ZGO-based anodes are compared in **Table S1** (see Supporting Information).

The highly enhanced electrochemical performance including high discharge capacity, long-term cycle life and excellent rate capability of the novel self-supported ZGO NSs@NF electrodes can be ascribed to the well-designed 3D self-supported porous network structure. First, using free-standing ultrathin ZGO NSs as building blocks and arranging them in a sponge-like structure increases the

available electrode-electrolyte contact area, which shortens the  $\text{Li}^+$  ion diffusion pathway and facilitates the electrochemical process.<sup>13, 65</sup> Second, the 3D interlinked ultrathin ZGO NSs with a self-supported structure can efficiently accommodate the stress induced by a drastic volume variation and avoid the structural collapse of active electrode materials on the repeated discharge/charge process as shown in **Figure 5**. The intumescent ZGO NSs resulting from the lithiation process were observed in **Figure 5E** on the initial five discharge/charge cycles at  $200 \text{ mA g}^{-1}$ . Even after 100 cycles, the interlinked 3D porous network structure can still be well-maintained in the self-supported ZGO NSs@NF composites (**Figure 5F**). For the same current density and cycle number, however, clear distortion, even severe fracture, of the ZGO NRs arrays from the NF substrate can be observed on the ZGO NRs@NF electrodes (**Figure 5K and 5L, and Figure S8A and S8B**, see Supporting Information), due to the limited tolerance to volume changes of the ZGO NRs. Third, the conductive NF skeleton not only prevents severe aggregation of the original ZGO NSs and the subsequent intermediate, which can improve the reversibility of the conversion reactions and facilitate the  $\text{Li}^+$  ion accessibility to the electrode,<sup>49, 51</sup> but also improves the electronic conductivity of the active materials in the total electrode even without other conductive additives. The Nyquist plots (**Figure S9**, see Supporting Information) show that the charge transfer resistance of the ZGO NSs@NF is lower than that of pristine ZGO flakes and ZGO NRs@NF. Just benefiting from these advantages, the novel self-supported ZGO NSs@NF anodes could demonstrate enhanced electrochemical cycling stability.

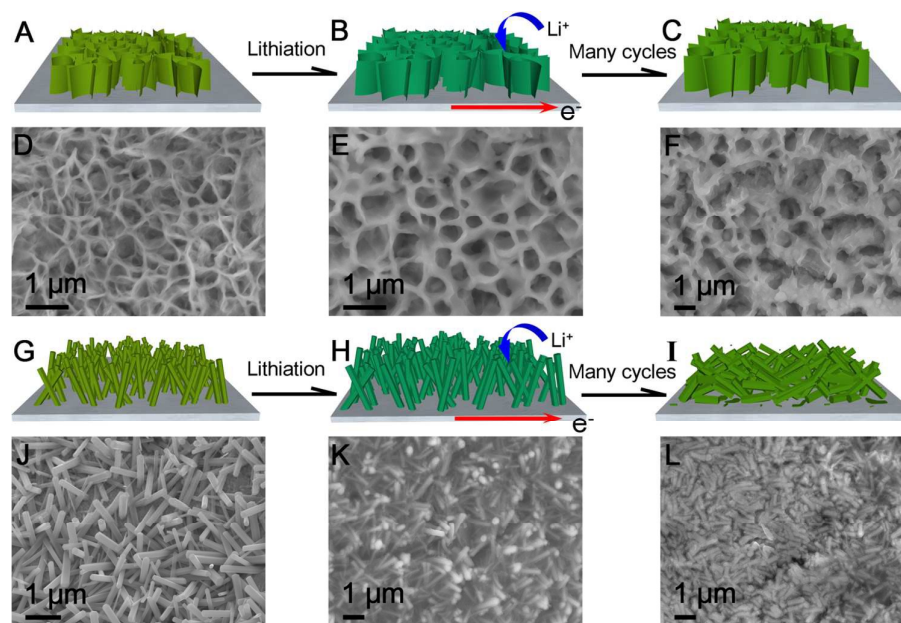


**Figure 5.** Schematic illustration of the buffer function of the interlinked ultrathin ZGO NSs (A, B, C) and ZGO NRs (G, H, I) on nickel foam during the lithiation/delithiation process. Initial FESEM (D, J) and post-mortem FESEM images (E, F, K, L) of ZGO NSs@NF and ZGO NRs after 5 cycles (E, K) and 100 cycles (F, L) at  $200 \text{ mA g}^{-1}$

## Journal Name

## COMMUNICATION

## Conclusions

In this paper, we successfully developed a novel hierarchical hybrid 3D self-supported structure composed of free-standing ultrathin ZGO NSs on conductive nickel foam (NF) through a simple CTAB-assisted hydrothermal process at 160 °C for 3 h. With the help of CTAB, the ultrathin ZGO NSs were interconnected and aligned vertically on the NF substrate to form a self-supported sponge-like network structure. This novel structure facilitated electronic/ionic transport and stabilized the total electrode structure upon the repeated cycling. The ZGO NSs@NF exhibited excellent electrochemical performance with a high discharge capacity, a long-term cycling stability and a good rate capability. A high reversible discharge capacity of about 794 mAh g<sup>-1</sup> was readily maintained after 500 cycles at a current density of 200 mA g<sup>-1</sup>, corresponding to an 81% capacity retention of second 2<sup>nd</sup> cycle. Even cycling at a higher current density of 2000 mA g<sup>-1</sup>, the novel ZGO NSs@NF still delivers a stable discharge capacity of 537 mAh g<sup>-1</sup>. Furthermore, the LiFePO<sub>4</sub>/ZGO NSs@NF full-cells also deliver a stable discharge capacity of 104 mA h g<sup>-1</sup> after 80 cycles. Such a self-supported structural construction of a 3D free-standing ultrathin NSs network on a conductive substrate could offer an excellent volume buffer effect and improve interfacial contacts, which may stimulate the progress of other energy-efficient technologies.

## Author contributions

G.G and Y.X fabricated the electrode materials and analysed the electrochemical performance. S.L., B.D. and C.S. contributed to SEM and TEM measurement. S.L. carried out XRD measurement. L.S. performed TGA and Y.W. performed BET tests. G.G and K.X. wrote the manuscript. All authors discussed the results. S.D. and K.X. supervised the project.

## Acknowledgements

This research was supported partially by the Fundamental Research Funds for the Central Universities (xjj2015119), the National Natural Science Foundation of China (No. 51273158, 21303131), the China Postdoctoral Science Foundation (No. 2016M592776) and the Natural Science Foundation of Shaanxi Province (No. 2016JM5021).

## References

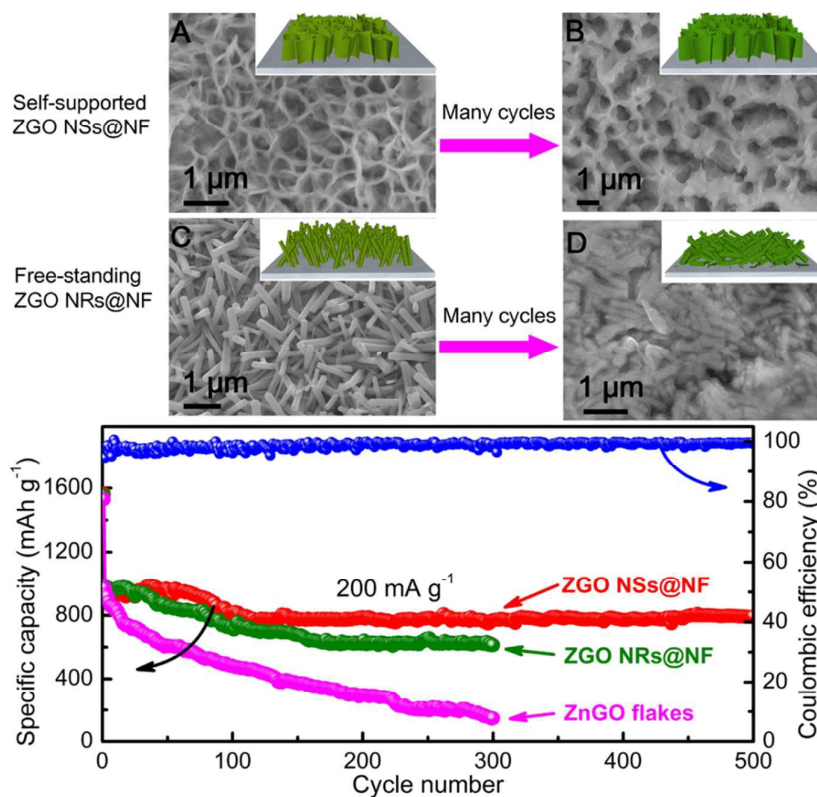
- N. Mahmood, T. Y. Tang and Y. L. Hou, *Adv. Energy Mater.*, 2016, **6**, 1600374.
- Z. Y. Wang, L. Zhou and X. W. Lou, *Adv. Mater.*, 2012, **24**, 1903-1911.
- H. B. Wu, J. S. Chen, H. H. Hng and X. W. Lou, *Nanoscale*, 2012, **4**, 2526-2542.
- F. Zhang and L. M. Qi, *Adv. Sci.*, 2016, **3**, 1600049.
- Z. S. Wu, W. C. Ren, L. Wen, L. B. Gao, J. P. Zhao, Z. P. Chen, G. M. Zhou, F. Li and H. M. Cheng, *ACS Nano*, 2010, **4**, 3187-3194.
- H. L. Wang, L. F. Cui, Y. A. Yang, H. S. Casalongue, J. T. Robinson, Y. Y. Liang, Y. Cui and H. J. Dai, *J. Am. Chem. Soc.*, 2010, **132**, 13978-13980.
- Y. S. Hu, R. Demir-Cakan, M. M. Titirici, J. O. Muller, R. Schlogl, M. Antonietti and J. Maier, *Angew. Chem. Int. Ed.*, 2008, **47**, 1645-1649.
- X. L. Wu, Y. G. Guo and L. J. Wan, *Chem. Asian. J.*, 2013, **8**, 1948-1958.
- D. T. Ngo, R. S. Kalubarme, H. T. T. Le, J. G. Fisher, C. N. Park, I. D. Kim and C. J. Park, *Adv. Funct. Mater.*, 2014, **24**, 5291-5298.
- J. Hwang, S. H. Woo, J. Shim, C. Jo, K. T. Lee and J. Lee, *ACS Nano*, 2013, **7**, 1036-1044.
- P. Poizot, S. Laruelle, S. Grugeon, L. Dupont and J. M. Tarascon, *Nature*, 2000, **407**, 496-499.
- Y. Z. Su, S. Li, D. Q. Wu, F. Zhang, H. W. Liang, P. F. Gao, C. Cheng and X. L. Feng, *ACS Nano*, 2012, **6**, 8349-8356.
- G. X. Gao, S. Y. Lu, Y. Xiang, B. T. Dong, W. Yan and S. J. Ding, *Dalton. Trans.*, 2015, **44**, 18737-18742.
- G. X. Gao, S. Y. Lu, B. T. Dong, W. Yan, W. Wang, T. Zhao, C. Y. Lao, K. Xi, V. Kumar and S. J. Ding, *J. Mater. Chem. A*, 2016, **4**, 10419-10424.
- G. Q. Zhang, B. Y. Xia, C. Xiao, L. Yu, X. Wang, Y. Xie and X. W. Lou, *Angew. Chem. Int. Ed.*, 2013, **52**, 8643-8647.
- X. L. Jia, Z. Chen, X. Cui, Y. T. Peng, X. L. Wang, G. Wang, F. Wei and Y. F. Lu, *ACS Nano*, 2012, **6**, 9911-9919.
- X. Xu, W. Liu, Y. Kim and J. Cho, *Nano Today*, 2014, **9**, 604-630.
- S. H. Choi and Y. C. Kang, *Small*, 2014, **10**, 474-478.
- S. P. Wu, C. P. Han, J. Iocozzia, M. J. Lu, R. Y. Ge, R. Xu and Z. Q. Lin, *Angew. Chem. Int. Ed.*, 2016, **55**, 7898-7922.
- Z. L. Hu, S. Zhang, C. J. Zhang and G. L. Cui, *Coord. Chem. Rev.*, 2016, **326**, 34-85.
- C. J. Zhang, F. L. Chai, L. Fu, P. Hu, S. P. Pang and G. L. Cui, *J. Mater. Chem. A*, 2015, **3**, 22552-22556.
- K. H. Seng, M. H. Park, Z. P. Guo, H. K. Liu and J. Cho, *Nano Lett.*, 2013, **13**, 1230-1236.
- H. Y. Qiu, L. X. Zeng, T. B. Lan, X. K. Ding and M. D. Wei, *J. Mater. Chem. A*, 2015, **3**, 1619-1623.
- Y. Wang and G. X. Wang, *Chem. Asian. J.*, 2013, **8**, 3142-3146.
- Z. Fang, T. T. Qiang, J. X. Fang, Y. X. Song, Q. Y. Ma, M. Ye, F. Q. Qiang and B. Y. Geng, *Electrochim. Acta*, 2015, **151**, 453-458.
- H. H. Li, L. L. Zhang, C. Y. Fan, X. L. Wu, H. F. Wang, X. Y. Li, K. Wang, H. Z. Sun and J. P. Zhang, *J. Mater. Chem. A*, 2016, **4**, 2055-2059.
- Z. Chen, Y. Yan, S. Xin, W. Li, J. Qu, Y. G. Guo and W. G. Song, *J. Mater. Chem. A*, 2013, **1**, 11404-11409.
- J. K. Feng, M. O. Lai and L. Lu, *Mater. Res. Bull.*, 2012, **47**, 1693-1696.
- S. P. Wu, R. Wang, Z. L. Wang and Z. Q. Lin, *Nanoscale*, 2014, **6**, 8350-8358.
- S. X. Jin and C. X. Wang, *Nano Energy*, 2014, **7**, 63-71.
- J. Feng, C. Wang and Y. Qian, *Mater. Lett.*, 2014, **122**, 327-330.

## COMMUNICATION

## Journal Name

- 32 W. W. Li, D. Chen and G. Z. Shen, *J. Mater. Chem. A*, 2015, **3**, 20673-20680.
- 33 T. Lv, X. Li and J. M. Ma, *RSC Adv.*, 2014, **4**, 49942-49945.
- 34 D. Li, C. Q. Feng, H. K. Liu and Z. P. Guo, *Sci. Rep.*, 2015, **5**, 11326.
- 35 F. Zhang, R. H. Zhang, Z. Zhang, H. K. Wang, J. K. Feng, S. L. Xiong and Y. T. Qian, *Electrochim. Acta*, 2014, **150**, 211-217.
- 36 Y. Subramanian, K. Kaliyappan and K. S. Ramakrishnan, *J. Colloid Interface Sci.*, 2017, **498**, 76-84.
- 37 W. Li, Y. X. Yin, S. Xin, W. G. Song and Y. G. Guo, *Energy Environ. Sci.*, 2012, **5**, 8007-8013.
- 38 F. Zou, X. L. Hu, Y. M. Sun, W. Luo, F. F. Xia, L. Qie, Y. Jiang and Y. H. Huang, *Chem. Eur. J.*, 2013, **19**, 6027-6033.
- 39 W. W. Li, X. F. Wang, B. Liu, J. Xu, B. Liang, T. Luo, S. J. Luo, D. Chen and G. Z. Shen, *Nanoscale*, 2013, **5**, 10291-10299.
- 40 Y. R. Lim, C. S. Jung, H. S. Im, K. Park, J. Park, W. I. Cho and E. H. Cha, *J. Mater. Chem. A*, 2016, **4**, 10691-10699.
- 41 X. Liu, J. Zai, B. Li, J. Zou, Z. Ma and X. Qian, *J. Mater. Chem. A*, 2016, **4**, 10552-10557.
- 42 R. Wang, S. P. Wu, Y. C. Lv and Z. Q. Lin, *Langmuir*, 2014, **30**, 8215-8220.
- 43 W. Wang, J. W. Qin and M. H. Cao, *ACS Appl. Mater. Interfaces*, 2016, **8**, 1388-1397.
- 44 L. Yu, R. Zou, Z. Zhang, G. Song, Z. Chen, J. Yang and J. Hu, *Chem. Comm.*, 2011, **47**, 10719-10721.
- 45 R. Yi, J. K. Feng, D. P. Lv, M. L. Gordin, S. R. Chen, D. W. Choi and D. H. Wang, *Nano Energy*, 2013, **2**, 498-504.
- 46 Y. M. Sun, X. L. Hu, J. C. Yu, Q. Li, W. Luo, L. X. Yuan, W. X. Zhang and Y. H. Huang, *Energy Environ. Sci.*, 2011, **4**, 2870-2877.
- 47 S. Yuan, X. L. Huang, D. L. Ma, H. G. Wang, F. Z. Meng and X. B. Zhang, *Adv. Mater.*, 2014, **26**, 2273-2279.
- 48 L. F. Shen, Q. Che, H. S. Li and X. G. Zhang, *Adv. Funct. Mater.*, 2014, **24**, 2630-2637.
- 49 G. X. Gao, H. B. Wu, S. J. Ding, L. M. Liu and X. W. Lou, *Small*, 2015, **11**, 804-808.
- 50 W. M. Chen, L. Y. Lu, S. Maloney, Y. Yang and W. Y. Wang, *Phys. Chem. Chem. Phys.*, 2015, **17**, 5109-5114.
- 51 W. M. Chen, S. Maloney and W. Y. Wang, *Electrochim. Acta*, 2015, **176**, 96-102.
- 52 W. W. Li, X. F. Wang, B. Liu, S. J. Luo, Z. Liu, X. J. Hou, Q. Y. Xiang, D. Chen and G. Z. Shen, *Chem. Eur. J.*, 2013, **19**, 8650-8656.
- 53 J. K. Feng, M. O. Lai and L. Lu, *Electrochem. Commun.*, 2011, **13**, 287-289.
- 54 J. S. Kim, A. Y. Kim, Y. W. Byeon, J. P. Ahn, D. Byun and J. K. Lee, *Electrochim. Acta*, 2016, **195**, 43-50.
- 55 Y. Feng, X. D. Li, Z. P. Shao and H. T. Wang, *J. Mater. Chem. A*, 2015, **3**, 15274-15279.
- 56 K. Y. Lin, B. J. Ma, W. G. Su and W. Y. Liu, *Appl. Surf. Sci.*, 2013, **286**, 61-65.
- 57 N. Zhang, S. X. Ouyang, T. Kako and J. H. Ye, *Chem. Comm.*, 2012, **48**, 1269-1271.
- 58 J. H. Huang, K. N. Ding, Y. D. Hou, X. C. Wang and X. Z. Fu, *ChemSusChem*, 2008, **1**, 1011-1019.
- 59 S. C. Yan, J. J. Wang and Z. G. Zou, *Dalton. Trans.*, 2013, **42**, 12975-12979.
- 60 G. X. Gao, H. B. Wu, B. T. Dong, S. J. Ding and X. W. Lou, *Adv. Sci.*, 2015, **2**, 1400014.
- 61 J. Liu, G. K. Zhang, J. C. Yu and Y. D. Guo, *Dalton. Trans.*, 2013, **42**, 5092-5099.
- 62 X. Ge, S. Y. Song and H. J. Zhang, *Crystengcomm*, 2012, **14**, 7306-7311.
- 63 S. H. Chen and D. L. Carroll, *J. Phys. Chem. B*, 2004, **108**, 5500-5506.
- 64 F. Zou, X. L. Hu, L. Qie, Y. Jiang, X. Q. Xiong, Y. Qiao and Y. H. Huang, *Nanoscale*, 2014, **6**, 924-930.
- 65 Q. Li, X. G. Miao, C. X. Wang and L. W. Yin, *J. Mater. Chem. A*, 2015, **3**, 21328-21336.
- 66 L. Zhang, X. F. Cao, Y. L. Ma, X. T. Chen and Z. L. Xue, *Crystengcomm*, 2010, **12**, 3201-3206.
- 67 G. X. Gao, H. B. Wu and X. W. Lou, *Adv. Energy Mater.*, 2014, **4**, 1400422.
- 68 J. Wang, J. Polleux, J. Lim and B. Dunn, *The Journal of Physical Chemistry C*, 2007, **111**, 14925-14931.
- 69 T. Brezesinski, J. Wang, S. H. Tolbert and B. Dunn, *Nat Mater*, 2010, **9**, 146-151.
- 70 Z. Hu, L. Wang, K. Zhang, J. Wang, F. Cheng, Z. Tao and J. Chen, *Angew. Chem. Int. Ed.*, 2014, **53**, 12794-12798.

## Graphical abstract



Self-supported ultrathin ZGO NSs are successfully fabricated on nickel foam via a simple CTAB-assisted hydrothermal process. Such a robust 3D sponge-like structure presents a strong electrochemical tolerance, thus delivering excellent lithium storage performance with high discharge capacity, long-term cycling stability and a good rate capability.